# Vibrational Relaxation and Energy Migration of *N*-Methylacetamide in Water: The Role of Nonbonded Interactions

Pierre-André Cazade, Florent Hédin, Zhen-Hao Xu, and Markus Meuwly*

Department of Chemistry, University of Basel, Klingelbergstrasse 80, 4056 Basel, Switzerland

S *Supporting Information*

ABSTRACT: Nonequilibrium molecular dynamics (MD) simulations together with physics-based force fields are used to follow energy flow between vibrationally excited *N*-methylacetamide (NMA) and water. The simulations are carried out with a previously validated force field for NMA, based on a multipolar representation of the electrostatics, and with a new fluctuating point charge model. For the water solvent, a flexible and a rigid model was employed to distinguish between the role of inter- and intramolecular degrees of freedom. On a 10 ps time scale about 90% of the available energy goes into the solvent. The remaining energy resides within internal NMA-degrees of freedom from where energy flow takes place on longer time scales. The total amount of energy transferred to the solvent on the 10 ps time scale does not depend on whether the water molecules are rigid or flexible during the simulations. Vibrational energy relaxation time scales include two regimes: one on the several 100 fs time scale and a longer one, ranging from 6 to 10 ps. This longer time scale agrees with previous simulations but overestimates the experimentally determined relaxation time by a factor of 2, which can be explained by the classical treatment of the vibrations. Including a previously determined quantum correction factor brings the long time scale into quite favorable agreement with experiment. Coupling to the bending vibration of the water molecules in H-bonding contact with the excited C=O chromophore is substantial. The equilibrium and nonequilibrium distribution of the bending angles of the water molecules in contact with the local oscillator are non-Gaussian, and one approaches the other on the subpicosecond time scale. Analysis of the water velocity distribution suggests that the C=O vibrational energy relaxes into the solvent water shells in an impulsive fashion on a picosecond time scale.
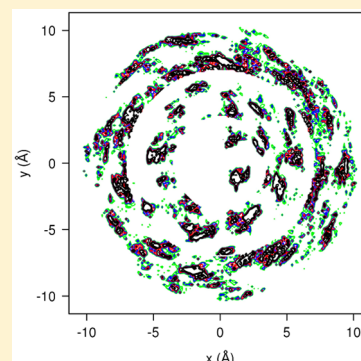
1. INTRODUCTION

The exchange of vibrational energy between molecules is important in understanding condensed phase phenomena because reaction rates and pathways are affected by energy exchange between solvent and solute.[1,2] Experimental and computational studies have been carried out for a variety of systems and situations, ranging from di- and triatomic molecules in different solvents[3–5] to CO in metal carbonyl compounds[6] and heme-bound CO in proteins.[7–9] Current progress in ultrafast time-resolved infrared and Raman spectroscopy applied to study intramolecular vibrational redistribution can provide details of the transient energy content of individual vibrations in solvated polyatomic molecules.[10–12] Such studies are complemented and their interpretation is aided by theoretical and computational work which allows one to follow the pathways of vibrational energy relaxation and redistribution.[1,13,14]

A rich dynamical picture has emerged from such investigations. The vibrational relaxation times were found to be typically on the few picosecond time scale and extending to the nanosecond or longer time regimes in exceptional cases, depending on the solvent, ligation state (e.g., bound versus unbound diatomic), and chemical environment of the spectroscopic probe.[2,5,15] Specifically, molecular dynamics (MD) simulations have provided considerable insight into

relaxation pathways and the role of intermolecular, in particular, electrostatic interactions. For example, the importance of electrostatic interactions has been investigated in quite some detail for a model dipolar molecule in a polar solvent.[16]

Compounds with peptide bonds have attracted particular interest because of their fundamental role in biological systems. The amide I mode, primarily associated with the peptide carbonyl stretch,[17] has been frequently used in experiments because its strong transition dipole makes it possible to identify its contributions.[10,18–22] This mode is of particular interest as it can be used to probe the topology and hydrogen-bond network through the intensity, spectral shift, and shape of this band.

The molecular system representing a peptide carbonyl most closely is *N*-methylacetamide (NMA; Figure 1). The vibrational relaxation of deuterated NMA (NMAD) in solution has been previously investigated in several experimental and theoretical studies,[10,11,23–25] which have provided a qualitative picture of the main relaxation pathways. However, differences in the interpretation of the vibrational energy decay and uncertainties in the experimental values of the relaxation lifetimes of the amide I mode show that a concise description of the vibrational
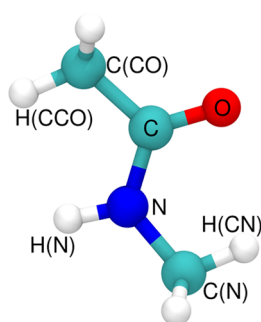
Figure 1. *N*-Methylacetamide molecule with atoms labeled.

relaxation of NMAD is still missing.[10,26] Recently, the heat transfer from NMA to various solvents has been investigated from temperature jump simulations.[27] This work employed a united-atom representation of NMA and found cooling times between 6 ps (water) and 28 ps (CCl₄). In addition, the sensitivity to nonbonded interactions (electrostatics and van der Waals) was investigated by scaling the strength of these contributions. However, the solvent structure and pathways for energy migration were not explicitly considered. Also, any anisotropy in the electrostatic interactions was absent because standard fixed-point charge models were employed.

Earlier work on the vibrational relaxation of NMA in D_2O using a united atom force field and nonequilibrium MD simulations found qualitative agreement with experiment for the rapid time scale of vibrational relaxation (1.5 ps versus 0.5 ps).[23] Using Fermi's golden rule, the vibrational relaxation time is 160 ps, which is 2 orders of magnitude longer than the experimental and nonequilibrium results.[23] A more recent study based on a multistep reaction and using non-Markovian time-dependent perturbation theory with the Neumann−Liouville equation and third-order Fermi resonance parameters to determine the mode-to-mode energy flow rate constants yields good agreement with the experimental results.[10,28] However, such an approach is limited to the subpicosecond time scale dynamics and does not provide a complete description of the relaxation process. Quantum effects on the amide I relaxation in NMA have also been investigated, and it was found that nonequilibrium MD simulations typically overestimate the picosecond relaxation time scale by a factor of 2 to 2.5, depending on how the classical MD simulations were carried out.[29] Yet another computational study used nonequilibrium dynamics of NMAD based on MD with quantum transitions in which the amide I mode is treated quantum mechanically while the remaining degrees of freedom are treated classically.[30] The instantaneous normal modes[31] of the initially excited NMAD molecule are used as internal coordinates. The time evolution of the energy stored in each individual normal mode is subsequently quantified using the hybrid quantum-classical instantaneous normal modes. Such an approach finds that amide I relaxation is dominated by intramolecular vibrational redistribution with little contribution from the solvent.

In the present study we aim at following the redistribution of the excitation energy for vibrational relaxation of the NMA−amide I mode in D_2O. Of particular interest are the modes and time scales for energy transfer into the surrounding solvent. On the basis of previous success for following vibrational relaxation of CN^- in D_2O from nonequilibrium MD simulations,[32] the present study uses high-quality force fields to investigate energy migration between vibrationally excited NMAD and the

surrounding D_2O solvent. The influence of the electrostatic model on the results is scrutinized, and the energy migration process is followed at atomic resolution. As NMA is a typical building block of polypeptides and proteins, the general insights regarding the relationship between force field accuracy, simulation strategy, and physicochemical observables is of great interest also in a wider context.

2. COMPUTATIONAL METHODS

2.1. Intermolecular Interactions. Force field parameters for NMA are based on CGenFF,[33] except for the C=O bonded term and electrostatics which are detailed below. For water, two models were considered: (i) the TIP3P model,[34] which is usually used for simulations in which the internal degrees of freedom are constrained, and (ii) the flexible Kumagai, Kawamura, and Yokokawa (KKY) model[32,35] to characterize the role of internal water degrees of freedom in the vibrational relaxation. The KKY potential correctly describes the harmonic frequencies of the water monomer and the infrared spectrum of liquid water[36] and has also been used successfully in characterizing the vibrational relaxation of solvated cyanide.[32]

Previous studies of vibrational relaxation in the condensed phase have shown that the nonbonded interactions are of fundamental importance for realistic simulations.[16,27,32,37] Here we decided to treat the electrostatics of the optically active C=O stretching mode with atom-centered fluctuating point charges (FPC). Such a model has already proved useful for investigations of the Stark effect of photodissociated ligands in Mb.[38−41] Alternatively, to more accurately describe electrostatic interactions, a multipolar (MTP) expansion can be used.[42,43] As the decomposition of the electron density into point charges and higher-order multipoles is not unique, the actual magnitudes of the multipoles can vary significantly. In previous work this was explored by designing three models with weak, medium, and strong multipoles (MTPW, MTPM, and MTPS, respectively) each of which is equally suitable to describe the electrostatics.[44] In the present work MTPW is used as it allows the most direct comparison with FPC because the vdW parameters are identical and the dipole and quadrupole moments are a perturbation compared to the CGenFF model.

All quantum chemical calculations in the present work were carried out with the Gaussian software.[45] For the fluctuating point charge model, the structure of NMA was first optimized at the B3LYP/aug-cc-pVQZ level of theory. Subsequently, the structure of NMA was distorted along the C=O bond length (*r*) and the partial atomic charges were determined by means of fitting to the electrostatic potential (ESP).[46,47] The *r*-grid included 21 distances between *r* = 1.1 Å and *r* = 1.35 Å. This choice was motivated by the amount of fluctuations of this coordinate in the MD simulations (~10% around the equilibrium). For each conformation, the charges obtained from the ESP analysis are represented as a linear expansion of the C=O bond length

$$q_X(r) = a_{X,0} + a_{X,1}r \tag{1}$$

where X stands for any atom of NMA. Using the B3LYP/aug-cc-pVQZ level of theory to determine the necessary electrostatic parameters was found to be reliable in previous work for NO, CN^-, O_2, or CO_2.[32,48−51] The results of the fitting procedure are shown in Table I in Supporting Information.

All bonded interaction terms are those of the CHARMM22 force field,[52] except for the C=O stretching potential, which was optimized in two steps. First, the parameters of the Morse potential $V(r) = D_e[1 - \exp(-\beta(r - r_e))]^2$ are fitted to electronic structure data (B3LYP/aug-cc-pVQZ). The parameters are then refined by reproducing the experimental gas phase C=O stretch frequency of 1731 cm^{-1} by adjusting D_e.[53] The final parameters are then $D_e = 120.47$ kcal/mol, $\beta = 2.174$ Å^{-1}, and $r_e = 1.294$ Å.

2.2. Molecular Dynamics Simulations. All MD simulations are carried out with CHARMM[54] using a time step of $\Delta t = 0.5$ fs when a flexible water model is employed and $\Delta t = 1$ fs when the water is constrained using SHAKE.[55] The equations of motion were propagated with the leapfrog algorithm. Periodic boundary conditions are applied in the three spatial directions, and a cutoff of 12 Å is used for the nonbonded interactions. A shifting and switching function is applied to electrostatic and van der Waals (vdW) interactions, respectively. Equilibration for the reference (equilibrium) trajectories is performed in the NVT ensemble at 300 K within the weak-coupling[56] limit with a damping constant of $\tau = 1.0$ ps for the thermostat. The reference and the relaxation simulations are run in the NVE ensemble. The reference trajectories are 2.5 ns long whereby data is stored every 10 ps for a total of 250 sets of $\mathbf{x}$ and $\mathbf{v}$. Positions ($\mathbf{x}$) and velocities ($\mathbf{v}$) are required to prepare the nonequilibrium state of the system (see below) and to follow the relaxation trajectories. The latter are carried out in two phases: during 2 ps after the excitation, the data is stored every 1 fs, and for the remaining 23 ps, the data is stored every 10 fs. This provides sufficient resolution for the early events after excitation and also allows one to follow further relaxation while keeping the amount of stored data manageable.

2.3. Vibrational Excitation. From the 250 sets ($\mathbf{x}$ and $\mathbf{v}$), the amide I IR mode of NMA is excited by depositing the corresponding energy (1725 cm^{-1} or 4.92 kcal/mol) as kinetic energy. This is achieved by suitably displacing the molecule along the C=O normal mode and scaling the velocity vector appropriately.[23] NMA is first reoriented in the (x,y) plane, providing the reorientation matrix $\mathbf{B}$. In this frame, the inertia tensor of NMA is calculated. In what follows, vectors and matrices are written in boldface while scalar numbers are in standard italic font. The scaled velocities ($\tilde{\mathbf{v}}$) are determined following the procedure outlined in eqs 2–5:

$$\tilde{\tilde{\mathbf{v}}} = \gamma(\mathbf{I}^\dagger \mathbf{B}^\dagger \mathbf{v} + \lambda \mathbf{L}(k)) \tag{2}$$

where $\mathbf{v}$ and $\mathbf{L}$ are the velocities of the current MD snapshot and the Cartesian displacements along the normal mode of interest, respectively. $\mathbf{B}$ is the rotation matrix in the NCO plane, and $\mathbf{I}$ is the matrix of the eigenvectors of the inertia matrix. $\tilde{\tilde{\mathbf{v}}}$ are the scaled velocities in the reoriented frame. The scaling factor λ is determined from

$$\lambda = \sqrt{\frac{2hc\nu}{\sum_i m_i(\mathbf{L}(k, i))^2}} \tag{3}$$

with ν is the wavenumber, m_i the mass of the atom i, and k the normal mode of interest. The scaling factor λ ensures that the energy deposited corresponds to excitation along the normal mode of interest. Adding the signed components of the normal mode vector and the instantaneous velocity $\mathbf{v}$ in general leads to a change of the total energy which does not correspond to the desired excitation, which is 4.92 kcal/mol in the present

case. Therefore, it is necessary to rescale the resulting velocity by a second factor γ

$$\gamma = \sqrt{\frac{2hc\nu + E_{kin}^0}{E_{kin}^\lambda}} \tag{4}$$

where E_{kin}^0 is the kinetic energy due to the velocities $\mathbf{v}$ and E_{kin}^λ the kinetic energy due to the increased velocities by the scaled normal mode, $\mathbf{I}^\dagger \mathbf{B}^\dagger \mathbf{v} + \lambda \mathbf{L}(k)$

$$\tilde{\mathbf{v}} = \mathbf{B} \mathbf{I} \tilde{\tilde{\mathbf{v}}} \tag{5}$$

$\tilde{\mathbf{v}}$ are the modified velocities along the normal mode used for IR excitation.

2.4. Data Analysis. For the present work it is of particular interest to follow the temporal evolution of various energy components. Their change relative to the initial state is obtained from

$$\Delta E(t) = \frac{1}{N} \sum_i^N \sum_j^M (E_{ij}^*(t) - E_{ij}^0) \tag{6}$$

where $N = 250$ corresponds to the number of trajectories and $M = 882$ to the number of water molecules. The superscripts $*$ and 0 refer to the excited and the reference trajectory, respectively.

3. RESULTS

In the following, results from atomistic simulations using several force field parametrizations for NMAD are discussed. One of them is a previously validated multipolar force field which correctly reproduces the pure liquid density and heat of vaporization along with the hydration free energy and the 2D infrared spectroscopy.[44] This is contrasted with simulations using a general-purpose (CGenFF) parametrization[33] and one which employs an FPC model (see Methods) to capture effects due to bond-polarizability.

3.1. Solvent Structure around the Chromophore. The local structure of water around NMA using the same force fields has been previously investigated.[44] The pair-correlation function between the oxygen atom of the carbonyl group of NMA and the water-O atoms exhibits a first peak at 2.8 Å, characteristic of a first water H-bonded shell. A second, weaker peak is found at about 5 Å. Such a one-dimensional description averages out several important features which become more prominent when considering two-dimensional water densities. They establish that three main regions can be distinguished: (i) a relatively high-density region close to the molecule (within the first 3.5 Å) corresponding to the first solvation shell; (ii) a region of moderate density at distances 5−8 Å away, corresponding to a second solvation shell; and finally (iii) beyond 8 Å more uniformly distributed water corresponding to the bulk. Within region (i), there are localized and well-defined areas of high density corresponding to H-bonding sites: 2 around the O atom of NMA and one around the NH group. The water-bonding sites around the C=O-group are of particular interest for the present work.

Inspection of the local solvation of the C=O-group shows that at the time of excitation the number (n_w) of water molecules H-bonded to the oscillator can vary between 0 and 4. The criterion for water proximity to the C=O group is that a water-oxygen atom (OW) was within 3 Å of the oxygen atom of NMA. For simulations with MTPW/KKY, the analysis of the 250 excitation trajectories yields $n_w = 0$ for 1% of the cases

compared to 37% in which n_w = 1, 52% with n_w = 2, and 10% with n_w = 3. This compares with 2% for n_w = 0, 35% in which n_w = 1, 55% with n_w = 2, 8% with n_w = 3, and below 1% for 4 water molecules when FPC/TIP3P is used. The lifetimes and energy relaxation characteristics for these different occupation states will be discussed further below.

3.2. Vibrational Relaxation Times. Vibrational energy relaxation of the excited NMA was monitored by following various energy components of the system.[27,32] This was done for simulations carried out with rigid (shaked TIP3P) and flexible (KKY) water molecules as the solvent and the MTPW and FPC models for NMAD.

3.2.1. Simulations with the MTPW Model. The MTPW model for NMAD has been previously validated in condensed-phase simulations of solvation free energies and spectroscopic properties.[44] A set of point dipole and quadrupole moments were attributed to each atom of NMAD. Ewald summation is used for the point charge electrostatics,[42,57] and all bonds involving H atoms are constrained with SHAKE. Excitation is carried out along the C=O-normal mode.

First, energy relaxation was followed by monitoring various energy components averaged over 250 independent trajectories from MTPW/TIP3P simulations, which are reported in Figure 2. For this, the total energy difference $\Delta E_{tot}^{NMA} = \Delta E_{kin}^{NMA} + \Delta E_{pot}^{NMA}$ of NMAD is considered and fit to a biexponential form

$$E(t) = a \, \exp\left(-\frac{t}{t_1}\right) + b \, \exp\left(-\frac{t}{t_2}\right) + c \tag{7}$$

However, it should be noted that sometimes biexponential fits have been found to be unstable or to sensitively depend on the initial guesses for the parameters.[27] Hence, single exponential fits of the long time scale have also been carried out separately. The vibrational relaxation time from analyzing the NMA total energy ΔE_{tot}^{NMA} is 8.7 ps from MTPW/TIP3P for the picosecond component, whereas the rapid component is 260 fs. The total energy of the system is almost constant, and rigorous energy conservation could be achieved by using a smaller time step in the *NVE*−MD simulations; see the discussion in ref 42. However, over the relevant time scale for vibrational relaxation ($\approx$ 10 ps), the total energy is well-conserved. Over the first 25 ps of the relaxation dynamics, the average kinetic energy of the water ΔE_{kin}^{WAT} increases by about 2 kcal/mol, which suggests that heating of the solvent following vibrational relaxation is not complete on this time scale.

3.2.2. Simulations with the FPC Model. Next, simulations with the FPC model are discussed. Here, a more detailed analysis is carried out. This is motivated by the fact that the results differ little compared to those of the more elaborate MTPW/TIP3P simulations (see below) which require dedicated parametrizations and coding and because it has been argued that polarizability could contribute to changes in the relaxation times[27] and a fluctuating multipole model was found to perform well for CN⁻.[32] A fluctuating point charge model is a first step toward such a polarizable model without, however, capturing effects of external polarization.

Figure 2 reports averaged (over the 250 trajectories) energy differences $\Delta E(t)$ between snapshots at the time of excitation $E(t = 0)$ and during the subsequent dynamics. For simulations with KKY, the total energy slightly fluctuates in the *NVE* ensemble. This fluctuation could again be reduced by using a smaller time step. However, we note that no drift in the total energy occurs, which underlines that the simulations are meaningful.

The total energy of water (cyan), it is found to increase as NMAD relaxes (indigo). The kinetic (orange) and potential (not shown) energy of the water molecules is, however, not equal as it was found for NMAD. This suggests that only part of the available energy is used to heat the solvent and the remaining energy goes into the configurational degrees of freedom of NMAD from where it relaxes on longer time scales. The interaction energy between NMAD and water, discussed further below, remains largely unchanged between the time before and after excitation.

Depending on the water model used in the simulations, the time scale on which water heating (i.e., water kinetic energy increase) occurs differs. This can be seen by comparing the orange traces in the middle and bottom panels of Figure 2 where on average ΔE_{kin}^{WAT} increases by 1.25 and 2.0 kcal/mol over 25 ps, respectively, when using a rigid TIP3P or a flexible KKY model. This amounts to a difference of about 30%. The time scale on which NMAD relaxes (red dashed line) and energy transport to the water occurs also differs to some extent. The longer time scale for this process is 9.1 ps for (FPC/TIP3P) and 7.6 ps for (FPC/KKY), see Table 1, which is a difference of close to 20%.

The decay times and amplitudes for excitation along the normal mode (NM) for the various models investigated in the present work are summarized in Table 1. In all cases, two time scales describe the vibrational relaxation. They include a rapid, subpicosecond time scale, which has an amplitude of approximately 10% of the total energy deposited, and a longer time scale with relaxation times ranging from 6 to 9 ps (except for (FPC/TIP3P-2), discussed further below) characterizing
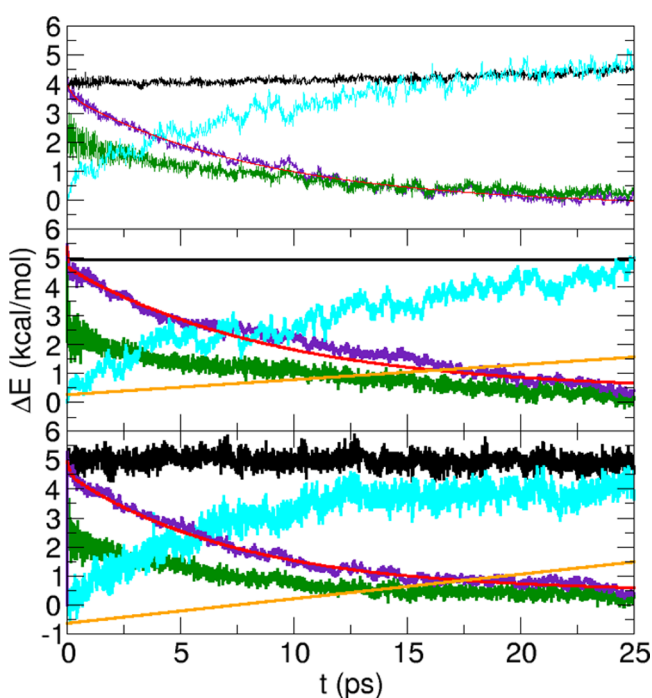

Figure 2. Averaged energy difference components from 250 individual nonequilibrium simulations for MTPW/TIP3P (top panel), FPC/TIP3P (middle panel), and FPC/KKY (bottom panel). Color code: ΔE_{tot} (black), ΔE_{tot}^{WAT} (cyan), ΔE_{tot}^{NMAD} (indigo) together with a two-time scales fit (red dashed), ΔE_{kin}^{WAT} (orange), and ΔE_{kin}^{NMAD} (green). For ΔE_{kin}^{WAT}, a linear fit (orange) is shown.

Table 1. Decay Times (Picoseconds) Exponential Fit of Potential and Kinetic Energies of NMAD in D$_2$O^a

	a (kcal/mol)	t_1 (ps)	b (kcal/mol)	t_2 (ps)	$t_2/2.5$ (ps)	c (kcal/mol)
			NM			
CGenFF/KKY	0.68	0.08	4.06	6.79	2.72	0.49
FPC/KKY	0.43	0.13	4.07	7.58	3.03	0.44
FPC/TIP3P	0.71	0.03	4.27	9.14	3.66	0.39
FPC/TIP3P-1	0.61	0.06	3.88	6.52	2.61	0.57
FPC/TIP3P-2	0.76	0.04	5.09	18.07	7.23	−0.56
FPC(+5%)/KKY^b	0.68	0.04	4.00	5.63	2.25	0.52
FPC(+7.5%)/KKY^b	0.39	0.46	4.21	7.60	3.04	0.23
MTPW/TIP3P	0.40	0.26	3.84	8.72	3.49	−0.24
			CO			
CGenFF/KKY	−	−	4.67	10.55	4.22	0.30
FPC/KKY	0.25	1.36	4.82	8.08	3.23	0.26
FPC/TIP3P	−	−	5.11	10.68	4.27	0.00
FPC(+5%)/KKY^b	−	−	4.72	7.81	3.12	0.48
FPC(+7.5%)/KKY^b	−	−	5.33	10.41	4.16	−0.25

^{a}Relaxation following normal mode (NM) or CO-bond (CO) excitation are separately reported. TIP3P-1 and TIP3P-2 analyze the data from the FPC/TIP3P trajectories but distinguish two subsets: one when a single water molecule is H-bonded to the carbonyl moiety (TIP3P-1), the second one for which two water molecules are H-bonded to the carbonyl moiety. ^{b}See Supporting Information; the column $t_2/2.5$ reports the long time scale accounted for quantum corrections.[29]
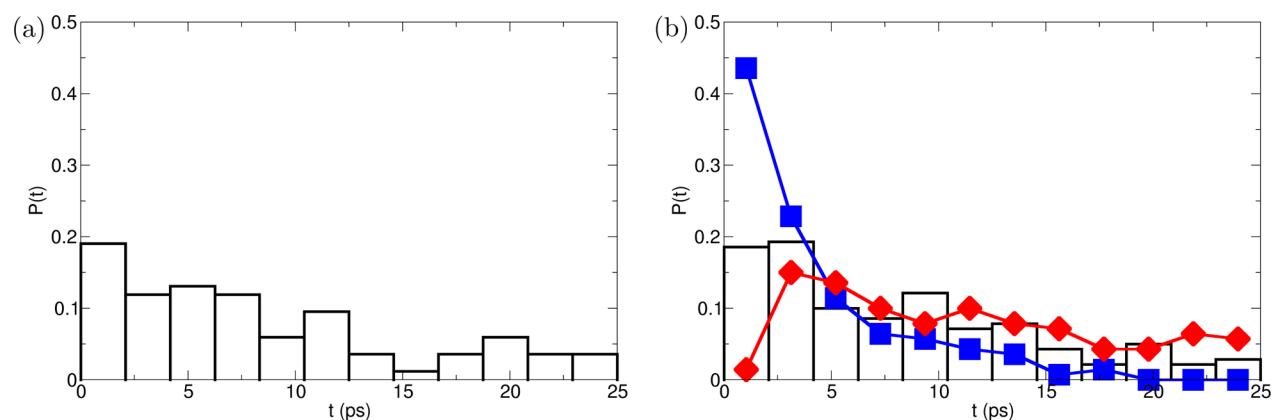

Figure 3. Probability distribution of the postexcitation lifetime of the H-bonded water molecules on the carbonyl group of NMA. (a) 1 H-bonded molecule; (b) 2 H-bonded molecules: (blue) shorter lifetime, (red) longer lifetime, and (black) distribution of the lifetime of the remaining molecule after the first left.

the genuine energy transfer process and is characterized by 90% of the amplitude.[58]

If vibrational excitation is induced by modification of the velocity vector along the C=O bond, energy relaxation is somewhat slower. Nevertheless, the time scale for relaxation is still around 10 ps and hence comparable to excitation along the normal mode.

3.2.3. Comparison with Previous Work. In experimental work[10,26] and previous atomistic simulations,[59] NMAD relaxation was found to involve up to 2 processes with different time scales when the normal mode is excited. Quantum and classical simulations of NMA relaxation by a nonequilibrium approach yield a relaxation time of 2.44 ps for the classical simulations when no zero-point correction is applied and 1.07 ps for the quantum simulations from which an empirical quantum correction factor was inferred.[29] In the present study, the number of time scales differed somewhat depending on which energy component was analyzed. The total energy of NMAD (potential plus kinetic energy) exhibits two relaxation time scales, whereas up to three time scales can be identified for the kinetic energy relaxation of NMA. In the former, the rapid component is on the femtosecond time scale (τ_1 = 40 to

460 fs), which compares favorably with the work by Cho and co-workers[26] and with Hochstrasser and co-workers[10] who find τ_1 = 450 fs comparable to the simulations by Cho and Jeon[59] who report a value of 620 fs. In both experiments and simulations, a second relaxation process on the picosecond time scale was reported, which is 4.0 ps[10] or 0.98 ps.[26] This long time scale is also found in the present work (see Table 1) and is somewhat larger than that of previous studies.[10,26] However, it agrees with results obtained by Jeon and Cho[59] where the longest time scale is 6.9 ps. In this study, the local CO mode (and not the normal mode) is excited and up to 3 time scales are found when fitting the NMA kinetic energy: 0.37, 2.3, and 6.9 ps. The latter component is found only for solvated NMA but not for NMA in the gas phase. This suggests that the short time scales involve relaxation processes within NMA while the long one involves transfer for NMA to the solvent. The present results also support the general observation that classical nonequilibrium MD simulations without zero-point energy overestimate the picosecond component of the vibrational relaxation time by a factor of 2−3 compared to experiment.[29]

3.2.4. Dynamics of Singly and Doubly H-Bonded C=O. As was mentioned above, at the moment of excitation, between

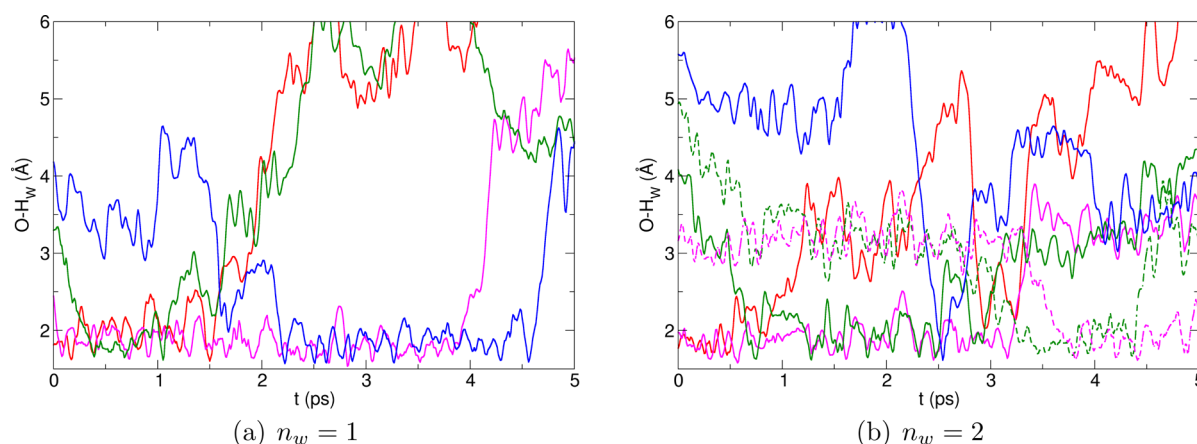(a) $n_w = 1$ (b) $n_w = 2$

Figure 4. $O_{NMA}-H_w$ separation of the water molecules closest to the NMA oxygen atom at $t = 0$. (left-hand side) $n_w = 1$; (right-hand side) $n_w = 2$. Dashed lines report the distance between O_{NMA} and the second H_w when a rotation of the water molecule is involved.
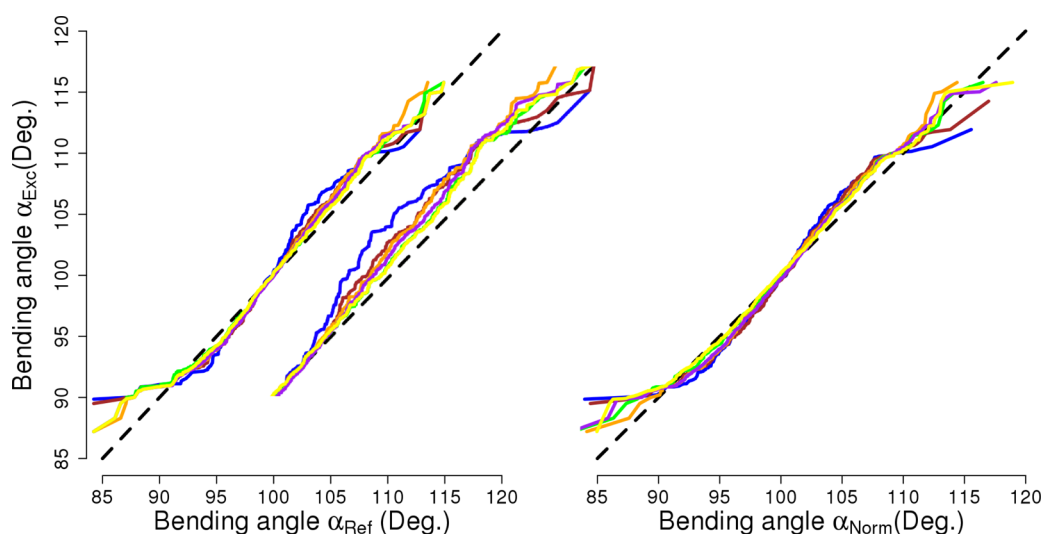

Figure 5. Q–Q plot for the water-bend-angle distribution of the closest three water molecules around the C=O group at the moment of excitation from one nonequilibrium simulation versus (left panel, α_{ref}) the three closest water molecules from an equilibrium simulation and (right panel, α_{Norm}) a Gaussian distribution. The color code refers to distributions from different times after vibrational excitation: 2.5 ps (blue), 5.0 ps (brown), 7.5 ps (orange), 10.0 ps (green), 12.5 ps (purple), and 15.0 ps (yellow). The data illustrates the nonequilibrium (left panel) and non-Gaussian (right panel) character of $p(\alpha)$ at early times (blue, brown). The black dashed line is for an ideal correlation between the nonequilibrium and the two reference distributions. The inset in the left panel shows a close-up for $\alpha_{ref} > 100°$.

$n_w = 0$ and 3 water molecules surround the C=O group, with $n_w = 1$ and $n_w = 2$ being the most probable situations. This allows the more detailed investigation of the subsequent dynamics depending on the initial configuration. First, the average lifetime of the water molecules in both situations is determined. For $n_w = 1$, the average water residence time is 9.6 ps, from which an approximate H-bond energy of 2.4 kcal/mol is inferred from $\Delta G_{AB} = -k_B T \ln \left(h/(k_B T \tau_{AB}) \right)$. When two water molecules are coordinated initially, the time for the first one to leave is 4.0 ps while on average the second water molecules remains H-bonded for 12.0 ps. This corresponds to an estimated H-bond energy of 1.9 and 2.6 kcal/mol, respectively.

Figure 3 reports the distribution of the postexcitation lifetime of the H-bonded water molecules to the CO group of NMA. The left-hand panel shows the distribution for $n_w = 1$. On the right-hand side, the case for $n_w = 2$ is shown: one trace is the distribution function for the first water to leave (blue), one for the molecules that survives the longest (red), and finally one for

the time the remaining molecule survives after the first left (black). The distributions between the two H-bonded molecules are different, illustrating the sequential renewal of the first solvation shell. Moreover, both distributions differ from the one obtained for a single bound molecule. Nevertheless, starting from $n_w = 2$ initially, the distribution of the lifetime of the second water molecule after the departure of the first one is similar to that for $n_w = 1$.

3.3. Solvent–Solute Energy Redistribution. The total energy change for NMAD ($\Delta E_{kin}^{NMA} + \Delta E_{pot}^{NMA}$) was analyzed in two ways. First, as an (unspecific) ensemble average over all 250 trajectories (i.e., the curve that would be obtained from experiment) and second, separately for those with $n_w = 1$ and $n_w = 2$ at the moment of excitation. Energy relaxation is more rapid for $n_w = 1$ compared to the unspecific ensemble average, whereas for $n_w = 2$ it is slower. As the proportion is approximately 1/3 and 2/3 for $n_w = 1$ and $n_w = 2$, respectively, weighting of the two relaxation curves should yield a decay close to that described by the ensemble average, which is also

what is found. Hence, depending on whether the C═O group is solvated by one or two water molecules at the moment of excitation, the relaxation behavior differs significantly.

It is also of interest to analyze the difference in the interaction energy between NMAD and the TIP3P water molecules between $t = 0$ and after vibrational excitation. Analysis of all 250 trajectories finds that this energy difference is close to 0 but slightly positive (see Figure S1 in Supporting Information), i.e., destabilizing. On the other hand, for the situation with $n_w = 1$, at the moment of excitation a stabilization of the system by ≈ 1.9 kcal/mol is found, whereas for $n_w = 2$ at the moment of excitation, the total interaction energy becomes slightly positive (≈ 0.5 kcal/mol), or destabilizing. Investigation of typical structures suggests that when starting from $n_w = 1$ (see red trace in Figure 4a), vibrational relaxation leads to rapid replacement of the H-bonded water molecule and a second water molecule forms an H-bond, which yields an overall stabilization because one strong H-bond is replaced by two somewhat weaker ones. On the other hand, when starting from $n_w = 2$, continuous exchange of water molecules leads to a more or less constant occupation by two water molecules; hence, the differential energy before and after vibrational excitation remains essentially unchanged.

3.3.1. Coupling between the C═O Stretch and the Water Bend. The only energetically feasible pathway between vibrationally excited NMAD and the internal solvent degrees of freedom is energy transfer to the water-bending mode. This is due to the proximity of the wavenumbers of the two modes which are at 1731 and 1595 cm^{-1} for NMA[53] and water, respectively. Such effects can be observed only when the water molecules in the simulations are flexible, which is the case for the KKY model. Involvement of internal solvent degrees of freedom have been mentioned but not quantified in previous work.[27] Nonequilibrium relaxation of the C═O local oscillator to a nearby (H-bonded) solvent molecule will lead to a bend-excited water molecule which subsequently relaxes. One characteristic of a nonequilibrium simulation is the fact that the distribution of a particular coordinate, for example, the bending angle $p(\alpha)$ of the water molecules, deviates from its equilibrium distribution. One convenient way to represent this are quantile−quantile (Q−Q) plots, which measure the deviation of a given distribution from a reference distribution, which is the equilibrium distribution of water-bending angles in the present case.[60] Such a Q−Q plot is shown in the left panel of Figure 5. It is evident that with increasing time (t) after vibrational excitation (represented by the color coding in Figure 5) the deviation from the reference distribution decreases and therefore approaches equilibrium. The same is true if the nonequilibrium distribution is compared with a Gaussian reference distribution, which is illustrated in the right-hand panel of Figure 5.

To better quantify and illustrate energy transfer to the water bending mode, the $p(\alpha)$ for the three closest water molecules around the C═O group at the moment of excitation was determined for 2.5, 5.0, 7.5, 10.0, 12.5, and 15.0 ps after excitation (Figure 6). As a reference, the three closest water molecules in an equilibrium simulation were analyzed in the same fashion. Both averaged distributions were fitted to a log-normal distribution

$$p(x) = \frac{k}{x} \exp\left(\frac{(\ln x - \mu)^2}{2\sigma^2} \right) \qquad (8)$$
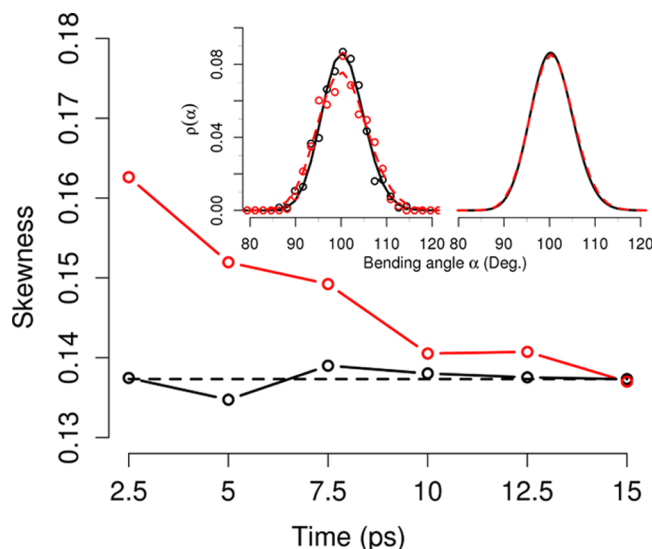

Figure 6. Insets report fitted probability distributions $p(\alpha)$ for the water-bending angle for the three closest water molecules at the time of excitation (red) and from equilibrium simulations (black). The $p(\alpha)$ are determined over increasing time intervals after the time of excitation, with the left panel for 2.5 ps and the right panel for 10.0 ps after excitation. The fits are log-normal distributions with residual sums of squares of 3.8×10^{-4} and 5.1×10^{-4} for the black and red curves in the left panel, respectively, and 1.1×10^{-4} and 6.7×10^{-5} in the right panel, respectively. The main figure reports the skewness as a function of time after excitation and confirms that the skewness in the vibrationally excited trajectories decreases as a function of time to a level corresponding to an equilibrium simulation.

where μ and σ are the mean and standard deviation of $\ln(\alpha)$, respectively; k is an overall scaling parameter, and the skewness parameter $(e^{\sigma^2} + 2)(e^{\sigma^2} - 1)^{1/2}$ is followed as a function of time after excitation. Both distributions have finite skewness, which implies that they are non-Gaussian. The nonequilibrium distribution has a larger skewness which decays toward the equilibrium value on the 10 ps time scale. Fitting the data to a reference Gaussian distribution also yields a satisfactory fit around the maximum of the data but deviates significantly in the wings.

Such an analysis does not provide detailed information about the time scale on which energy is transferred from the vibrationally excited NMAD to the surrounding water molecules. All that can be said is that it must be shorter than 2.5 ps. As a certain amount of data is required for reliable statistics on $p(\alpha)$, extending this analysis to shorter time scales is usually not meaningful because of increased uncertainties due to the small data sets available at short times after excitation.

3.4. Energy Migration. Atomistic simulations are particularly useful for characterizing quantities that are not directly observable experimentally. One such property is energy transfer in an energized system. For the present case a direct measure for energy migration can be obtained from analyzing the water velocity distribution $\rho_v(\mathbf{r},t)$ before and after excitation. In the following (eq 9) averages of the velocity vector amplitude density are discussed.

$$\rho_v(\mathbf{r}, t) = \langle \| \mathbf{v}(\mathbf{r}, t) \| \rangle = \frac{1}{N_t} \sum_{i=1}^{N_t} \mathbf{v}(\mathbf{r}, i) \qquad (9)$$

Here, N_t is the number of frames over which the absolute value of the velocity vector is averaged (i.e., averaging over $\Delta t =$
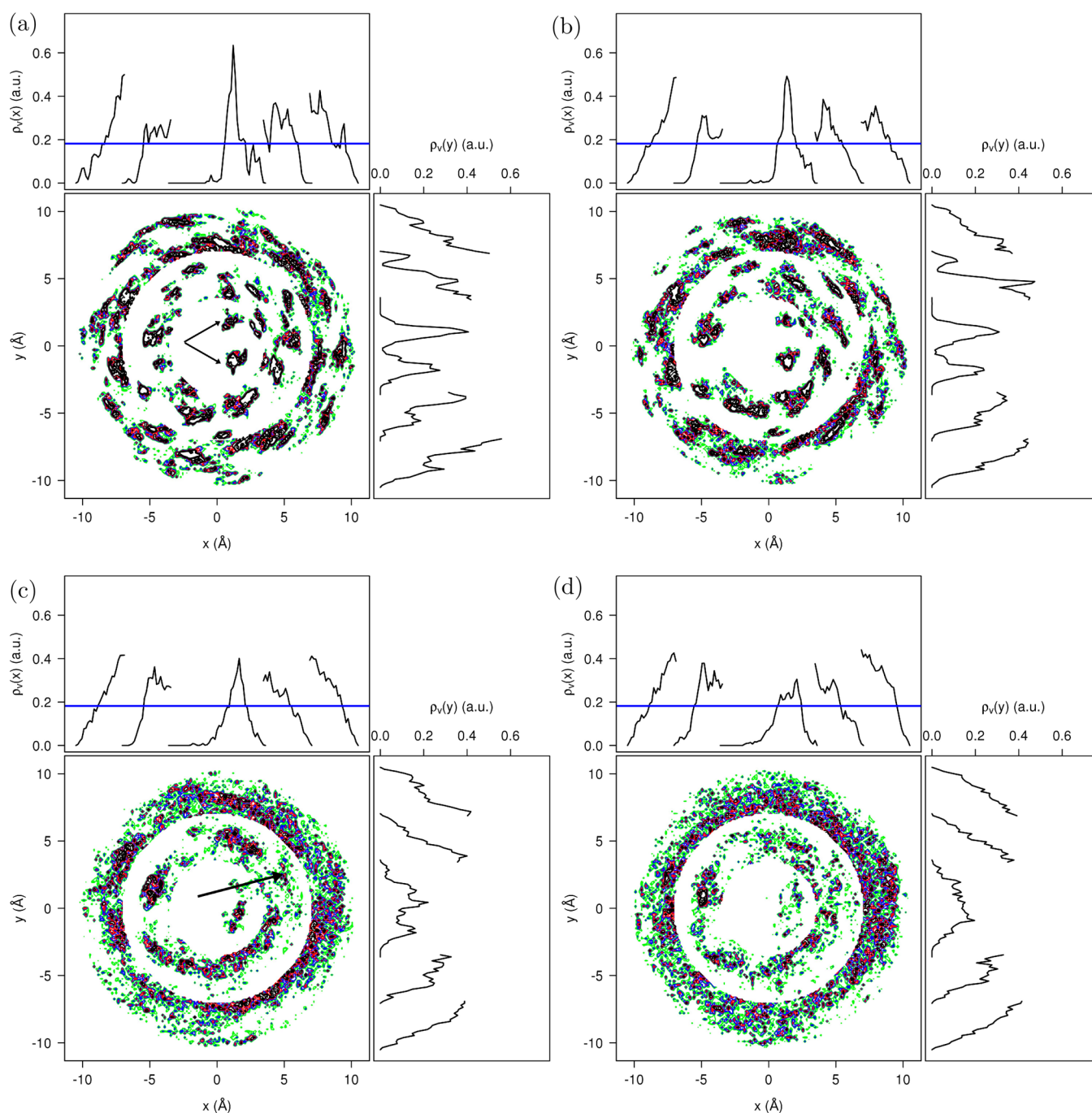
Figure 7. Isocontours of water velocity distribution amplitude as a function of simulation time from the nonequilibrium part of the trajectory. The color code is as follows: white (0.0−0.3), green (0.3−0.35), blue (0.4−0.45), red (0.5−0.55), and black (0.6−1.0). The black curves are the projection of the velocity density amplitude. The concentric circles are a consequence of analyzing water molecules in their respective solvent shells (see text). The horizontal blue line is to guide the eye, and the arrows point toward features discussed in the text.

0.25 ps); the index ν in ρ_{v} refers to the distribution of velocity vector amplitudes, and the quantity ρ_{v} contains information about the total solvent kinetic energy.

Figure 7 and Figure S2 in Supporting Information report amplitude densities of the water velocity distributions from nonequilibrium and equilibrium simulations, respectively. For this, the NMA-oxygen atom is the origin (0/0) of the coordinate system with the C=O group pointing along the +x-axis. The water shells, determined in recent work from $g(r)$,[44] are defined as follows: first shell within 3.5 Å of the NMA-oxygen atom; second shell between 3.5 and 7.0 Å of the

NMA-oxygen atom; third shell between 7.0 and 10.5 Å of the NMA-oxygen atom. Such a procedure leads to the concentric circles in Figure S2 and Figure 7 instead of homogeneous distributions but allow the representation of relative changes between magnitudes and granularity of the velocity amplitude distributions. The spatial resolution of the grid is 0.15 Å, and the density is averaged over 25 consecutive frames (0.25 ps in total) to provide sufficient time resolution but at the expense of a relatively low spatial resolution. NMA is drawn (see Figure S2) to indicate its orientation. On the top and the right-hand side of each contour, the projection of the density on the

corresponding axis is shown. The black curves correspond to x- and y-projections of the velocity amplitude density. The distributions within each shell are quite homogeneous and stationary $\rho_v(\mathbf{r},t)$ (eq 9) as a function of time.

The situation changes considerably after vibrational excitation at $t = 0$. The nonequilibrium relaxation of the water velocity density amplitude (eq 9) at times $t = 0.25$, 0.50, 0.75, and 1.0 ps after excitation is reported in Figure 7. During vibrational relaxation, energy migration within the water shells is obvious, as can be seen from comparing Figure S2 in Supporting Information and Figure 7d with Figure 7a−c. Energy migration is evident by the localized high-velocity peaks (black and dark areas in the contour plots) at early time which diminish as a function of time. The projections clearly show the propagation of the excess energy from NMA to the water molecules H-bonded to the carbonyl group (located at $x \approx 0$ and indicated by an arrow in Figure 7a) and then further toward the rest of the first solvation shell. As an example, the projection of the velocity amplitude distribution function in the first solvation shell during equilibrium dynamics is $\rho_v \approx 0.4$, whereas at 0.25 ps after vibrational excitation it has increased to $\rho_v = 0.7$. Over the course of the ensuing relaxation dynamics this peak decreases to the equilibrium value on the 1 ps time scale (Figure 7d).

Detailed consideration of the maximum amplitude in the first and second solvation shells along the positive x-axis (i.e., along the C=O bond) in Figure 7 also suggests that local heating takes place. This can be seen in the decrease of the maximum value of ρ_v in the first solvation shell as a function of time with concomitant increase in the same quantity for the second solvation shell. These features are equally pronounced when considering the projections along the y-direction. Also, contrary to the equilibrium situation, the concentric rings of the velocity density are distorted and a density maximum emerges at $x \approx 5$ Å. Moreover, the fact that the density of the averaged velocity vector $\rho_v(\mathbf{r},t)$ (not shown) is smaller than the vector amplitude, $\rho_v(\mathbf{r},t)$, indicates that shortly after excitation water molecules have disordered velocity vectors. This differs from the equilibrium trajectory where because of the slowly varying H-bonding pattern the averaged velocity vectors and their amplitude are similar. Within 1 ps most of the local energy redistribution around the C=O group is completed; however, the dynamics and energy exchange continues.

Integrating the velocity density over the first and second solvation shells (as indicated by the blue dashed lines in Figure S2 in Supporting Information) as a function of time after excitation suggests that energy migrates in a shock-wave-like fashion outward. This is illustrated in Figure 8. During the first picosecond, the integrated velocity density $S(\rho_v(\mathbf{r},t))$ in the first solvation shell decreases (black−red−green−blue), whereas in the second solvation shell $S(\rho_v(\mathbf{r},t))$ typically increases (largest for 0.50 and 0.75 ps after excitation and smaller for 0.25 and 1.0 ps). Hence, energy transfer between the two shells considered occurs on the 500 fs time scale. The fact that the velocity density decreases again after 1 ps suggests that energy is further transported into subsequent solvent layers.

4. CONCLUSIONS

The vibrational relaxation of NMA in the amide I region was investigated from atomistic simulations with validated force fields. Excitation along both the normal and the local C=O mode were considered. The two relaxation time scales are typically on the subpicosecond time scale and between 6 and
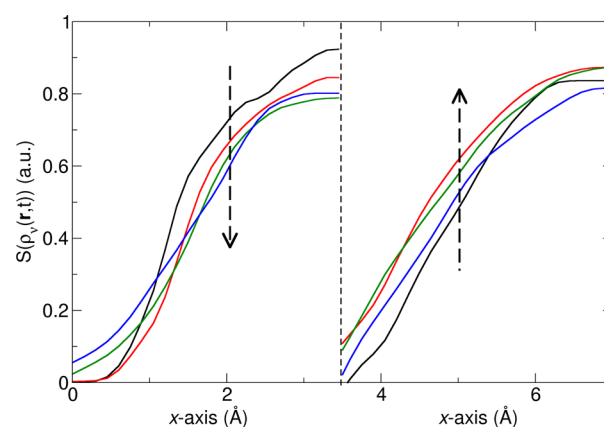

Figure 8. Integrated projections $S(\rho_v(\mathbf{r}, t))$ of $\rho_v(\mathbf{r}, t)$ onto the x-axis (see Figure 7) within the first (left panel) and second shell (right panel). For definition, see caption to Figure 7. The four times after excitation [0.25 ps (black), 0.50 ps (red), 0.75 ps (green), and 1.00 ps (blue)] are shown.

10 ps. Depending on the water model used in the simulations (flexible KKY or rigid/shaked TIP3P), the time scale on which water heating (i.e., water kinetic energy increase) occurs differs by about 30% with the faster pathway being the one which allows inter- and intramolecular relaxation. Furthermore, the fact that bifurcation (inter- versus intramolecular) in the relaxation pathway can occur is reminiscent of bifurcating pathways in reactivity as has been previously observed.[61] Energy transfer to the solvent has been followed by considering the two-dimensional velocity distribution of the surrounding water molecules. A nonequilibrium distribution can be clearly identified at early times (0.25 ps) after vibrational excitation which decays toward an equilibrium state on the picosecond time scale. The ensuing nonequilibrium distribution in the bending angles of the water molecules H-bonded to the chromophore at the time of excitation decays on a picosecond time scale. Depending on the H-bonding pattern of the solvent molecules closest to the C=O group, different kinetics is found for the water dynamics after vibrational excitation. For $n_w = 1$, which makes up $\approx$33% of the population, the average lifetime is 9.6 ps, whereas for $n_w = 2$ (56% of the population), two lifetimes (4.0 and 12.0 ps) were found. Experimentally, a superposition of the relaxation dynamics of these two states is observed. The results for the different force fields of the present work, the sensitivity analysis (see Supporting Information), and the results from previous work which considered vibrational energy relaxation in NMA and different solvents[27] suggest that vibrational relaxation times are not sufficiently sensitive for detailed force field refinements.

In summary, the present work provides an atomistically resolved picture of the vibrational relaxation of NMA and subsequent solvent dynamics. When quantum corrections[29] for the long (picosecond) time scale are accounted for, the simulation results quantitatively agree with experiment. Analysis of energy migration pathways shows that vibrational relaxation of NMA exhibits subpicosecond dynamics resulting in impulsive propagation of the excess energy into the surrounding solvent followed by excitation of the water-bending mode on the picosecond time scale.

■ ASSOCIATED CONTENT

Ⓢ Supporting Information

Electrostatic parameters for NMA; averaged water−NMA interaction energy from 250 nonequilibrium runs from FPC/TIP3P and FPC/KKY simulations; isocontours of water velocity distribution amplitude as a function of simulation time from the equilibrium part of the trajectory; and total energy difference for NMA and water for different modified force field parametrizations. This material is available free of charge via the Internet at http://pubs.acs.org.

■ AUTHOR INFORMATION

Notes

The authors declare no competing financial interest.

■ ACKNOWLEDGMENTS

■ REFERENCES

(1) Oxtoby, D. *Vibrational Relaxation in Liquids.* **1981**, *32*, 77−101.

(2) Stratt, R.; Maroncelli, M. Nonreactive dynamics in solution: The emerging molecular view of solvation dynamics and vibrational relaxation. *J. Phys. Chem.* **1996**, *100*, 12981−12996.

(3) Heilweil, E. J.; Doany, F. E.; Moore, R.; Hochstrasser, R. M. Vibrational Energy Relaxation of the Cyanide Ion in Aqueous Solution. *J. Chem. Phys.* **1982**, *76*, 5632−5634.

(4) Li, M.; Owrutsky, J.; Sarisky, M.; Culver, J. P.; Yodh, A.; Hochstrasser, R. M. Vibrational and rotational relaxation times of solvated molecular ions. *J. Chem. Phys.* **1993**, *98*, 5499−5507.

(5) Egorov, S.; Skinner, J. Vibrational energy relaxation of polyatomic solutes in simple liquids and supercritical fluids. *J. Chem. Phys.* **2000**, *112*, 275−281.

(6) Heilweil, E. J.; Cavanagh, R. R.; Stephenson, J. C. Population Relaxation of Co(v = 1) Vibrations in Solution Phase Metal Carbonyl Complexes. *Chem. Phys. Lett.* **1987**, *134*, 181−188.

(7) Sagnella, D. E.; Straub, J. E.; Jackson, T. A.; Lim, M.; Anfinrud, P. A. Vibrational Population Relaxation of Carbon Monoxide in the Heme Pocket of Photolyzed Carbonmonoxy Myoglobin: Comparison of Time-Resolved mid-IR Absorbance Experiments and Molecular Dynamics Simulations. *Proc. Natl. Acad. Sci. U.S.A.* **1999**, *96*, 14324−14329.

(8) Owrutsky, J. C.; Li, M.; Locke, B.; Hochstrasser, R. M. Vibrational Relaxation of the CO Stretch Vibration in Hemoglobin-Co, Myoglobin-Co, and Protoheme-Co. *J. Phys. Chem.* **1995**, *99*, 4842−4846.

(9) Mizutani, Y.; Kitagawa, T. Ultrafast dynamics of myoglobin probed by time-resolved resonance Raman spectroscopy. *Chem. Rec.* **2001**, *1*, 258−275.

(10) Hamm, P.; Lim, M.; Hochstrasser, R. M. Structure of the Amide I Band of Peptides Measured by Femtosecond Nonlinear-Infrared Spectroscopy. *J. Phys. Chem. B* **1998**, *5647*, 6123−6138.

(11) Zanni, M. T.; Asplund, M. C.; Hochstrasser, R. Two-Dimensional Heterodyned and Stimulated Infrared Photon Echoes of N-Methylacetamide-D. *J. Chem. Phys.* **2001**, *114*, 4579−4590.

(12) Hamm, P.; Helbing, J.; Bredenbeck, J. Two-Dimensional Infrared Spectroscopy of Photoswitchable Peptides. *Annu. Rev. Phys. Chem.* **2008**, *59*, 291−317.

(13) Owrutsky, J. C.; Raftery, D.; Hochstrasser, R. M. Vibrational-Relaxation Dynamics in Solutions. *Annu. Rev. Phys. Chem.* **1994**, *45*, 519−555.

(14) Lawrence, C. P.; Skinner, J. L. Vibrational spectroscopy of HOD in liquid D_2O. III. Spectral diffusion, and hydrogen-bonding and rotational dynamics. *J. Chem. Phys.* **2003**, *118*, 264−272.

(15) Devereux, M.; Meuwly, M. Force Field Optimization Using Dynamics and Ensemble Averaged Data: Vibrational Spectra and Relaxation in Bound MbCO. *J. Chem. Inf. Model.* **2010**, *50*, 349−357.

(16) Rey, R.; Hynes, J. T. Vibrational Phase and Energy Relaxation of CN^- in Water. *J. Chem. Phys.* **1998**, *108*, 142−153.

(17) Krimm, S.; Bandekar, J. Vibrational Spectroscopy and Conformation of Peptides, Polypeptides, and Proteins. *Adv. Protein Chem.* **1986**, *38*, 181.

(18) Peterson, K. A.; Rella, C. W.; Engholm, J. R.; Schwettman, H. A. Ultrafast Vibrational Dynamics of the Myoglobin Amide I Band. *J. Phys. Chem. B* **1999**, *103*, 557−561.

(19) Moran, A.; Park, S.-M.; Mukamel, S. Infrared Photon Echo Signatures of Hydrogen Bond Connectivity in the Cyclic Decapeptide Antamanide. *J. Chem. Phys.* **2003**, *118*, 9971−9980.

(20) Moran, A.; Mukamel, S. The Origin of Vibrational Mode Couplings in Various Secondary Structural Motifs of Polypeptides. *Proc. Natl. Acad. Sci. U.S.A.* **2004**, *101*, 506−510.

(21) Xie, A.; van der Meer, L.; Hoff, W.; Austin, R. H. Long-Lived Amide I Vibrational Modes in Myoglobin. *Phys. Rev. Lett.* **2000**, *84*, 5435−5438.

(22) Austin, R. H.; Xie, A.; van der Meer, L.; Redlich, B.; Lindgard, P. A.; Frauenfelder, H.; Fu, D. Picosecond Thermometer in the Amide I Band of Myoglobin. *Phys. Rev. Lett.* **2005**, *94*, 128101.

(23) Nguyen, P. H.; Stock, G. Nonequilibrium molecular-dynamics study of the vibrational energy relaxation of peptides in water. *J. Chem. Phys.* **2003**, *119*, 11350−11358.

(24) Corcelli, S. A.; Lawrence, C. P.; Skinner, J. L. Combined Electronic Structure/Molecular Dynamics Approach for Ultrafast Infrared Spectroscopy of Dilute HOD in Liquid H_2O and D_2O. *J. Chem. Phys.* **2004**, *120*, 8107−8117.

(25) Hayashi, T.; Zhuang, W.; Mukamel, S. Electrostatic DFT Map for the Complete Vibrational Amide Band of NMA. *J. Phys. Chem. A* **2005**, *109*, 9747−9759.

(26) Decamp, M. F.; Deflores, L.; Mccracken, J. M.; Tokmakoff, A.; Kwac, K.; Cho, M. Amide I Vibrational Dynamics of N-Methylacetamide in Polar Solvents: The Role of Electrostatic Interactions. *J. Phys. Chem. B* **2005**, *109*, 11016−11026.

(27) Park, S.-M.; Nguyen, P. H.; Stock, G. Molecular dynamics simulation of cooling: Heat transfer from a photoexcited peptide to the solvent. *J. Chem. Phys.* **2009**, *131*.

(28) Zhang, Y.; Fujisaki, H.; Straub, J. E. Mode-Specific Vibrational Energy Relaxation of Amide I′ and II″ Modes in N-Methylacetamide/Water Clusters: Intra- and Intermolecular Energy Transfer Mechanisms. *J. Phys. Chem. A* **2009**, *113*, 3051−3060.

(29) Stock, G. Classical Simulation of Quantum Energy Flow in Biomolecules. *Phys. Rev. Lett.* **2009**, *102*, 118301.

(30) Bastida, A.; Soler, M. A.; Zuniga, J.; Requena, A.; Kalstein, A.; Fernandez-Alberti, S. Hybrid Quantum/Classical Simulations of the Vibrational Relaxation of the Amide I Mode of N-Methylacetamide in D_2O Solution. *J. Phys. Chem. B* **2012**, *116*, 2969−2980.

(31) David, E. F.; Stratt, R. M. The anharmonic features of the short-time dynamics of fluids: The time evolution and mixing of instantaneous normal modes. *J. Chem. Phys.* **1998**, *109*, 1375−1390.

(32) Lee, M. W.; Meuwly, M. On the Role of Nonbonded Interactions in Vibrational Energy Relaxation of Cyanide in Water. *J. Phys. Chem. A* **2011**, *115*, 5053−5061.

(33) Vanommeslaeghe, K.; Hatcher, E.; Acharya, C.; Kundu, S.; Zhong, S.; Shim, J.; Darian, E.; Guvench, O.; Lopes, P.; Vorobyov, I.; Mackerell, A. D., Jr. CHARMM General Force Field: A Force Field for Drug-Like Molecules Compatible with the CHARMM All-Atom Additive Biological Force Fields. *J. Comput. Chem.* **2010**, *31*, 671−690.

(34) Jorgensen, W. L.; Chandrasekhar, J.; Madura, J. D.; Impey, R. W.; Klein, M. L. Comparison of simple potential functions for simulating liquid water. *J. Chem. Phys.* **1983**, *79*, 926−935.

(35) Kumagai, N.; Kawamura, K.; Yokokawa, T. An Interatomic Potential Model for H_2O: Applications to Water and Ice Polymorphs. *Mol. Simul.* **1994**, *12*, 177−186.

(36) Gupta, P. K.; Meuwly, M. Dynamics and vibrational spectroscopy of water at hydroxylated silica surfaces. *Faraday Discuss.* **2013**, *167*, 329−346.

(37) Danielsson, J.; Meuwly, M. Energetics and Dynamics in MbCN: CN⁻-Vibrational Relaxation from Molecular Dynamics Simulations. *J. Phys. Chem. B* **2007**, *111*, 218−226.

(38) Nutt, D. R.; Meuwly, M. Theoretical Investigation of Infrared Spectra and Pocket Dynamics of Photodissociated Carbonmonoxy Myoglobin. *Biophys. J.* **2003**, *85*, 3612−3623.

(39) Plattner, N.; Meuwly, M. The Role of Higher CO-Multipole Moments in Understanding the Dynamics of Photodissociated Carbonmonoxide in Myoglobin. *Biophys. J.* **2008**, *94*, 2505−2515.

(40) Lutz, S.; Nienhaus, K.; Nienhaus, G. U.; Meuwly, M. Ligand Migration Between Internal Docking Sites in Photodissociated Carbonmonoxy Neuroglobin. *J. Phys. Chem. B* **2009**, *113*, 15334−15343.

(41) Plattner, N.; Meuwly, M. Quantifying the Importance of Protein Conformation on Ligand Migration in Myoglobin. *Biophys. J.* **2012**, *102*, 333−341.

(42) Bereau, T.; Kramer, C.; Meuwly, M. Leveraging Symmetries of Static Atomic Multipole Electrostatics in Molecular Dynamics Simulations. *J. Chem. Theory Comput.* **2013**, *9*, 5450−5459.

(43) Kramer, C.; Gedeck, P.; Meuwly, M. Atomic Multipoles: Electrostatic Potential Fit, Local Reference Axis Systems and Conformational Dependence. *J. Comput. Chem.* **2012**, *33*, 1673−1688.

(44) Cazade, P.-A.; Bereau, T.; Meuwly, M. Computational Two-Dimensional Infrared Spectroscopy without Maps: *N*-Methylacetamide in Water. *J. Phys. Chem. B* **2014**, *118*, 8135−8147.

(45) Frisch, M. J.; Trucks, G. W.; Schlegel, H. B. et al., *Gaussian 03*, revision B.01; Gaussian, Inc.: Wallingford, CT, 2003.

(46) Singh, U. C.; Kollman, P. A. An Approach to Computing Electrostatic Charges for Molecules. *J. Comput. Chem.* **1984**, *5*, 129−145.

(47) Besler, B. H.; Merz, K. M.; Kollman, P. A. Atomic Charges Derived from Semiempirical Methods. *J. Comput. Chem.* **1990**, *11*, 431−439.

(48) Nutt, D. R.; Karplus, M.; Meuwly, M. Potential Energy Surface and Molecular Dynamics of MbNO: Existence of an Unsuspected FeON Minimum. *J. Phys. Chem. B* **2005**, *109*, 21118−21125.

(49) Nutt, D. R.; Meuwly, M. Ferric and Ferrous Iron in Nitroso-Myoglobin: Computer Simulations of Stable and Metastable States and their Infrared Spectra. *ChemPhysChem* **2007**, *8*, 527−536.

(50) Mishra, S.; Meuwly, M. Atomistic Simulation of NO Dioxygenation in Group I Truncated Hemoglobin. *J. Am. Chem. Soc.* **2010**, *132*, 2968−82.

(51) Cazade, P.-A.; Meuwly, M. Oxygen Migration Pathways in NO-bound Truncated Hemoglobin. *ChemPhysChem* **2012**, 4276−4286.

(52) A. D. Mackerell, J.; Bashford, D.; Bellott, M.; R. L. Dunbrack, J.; Evan-Seck, J. D.; Field, M. J.; Fischer, S.; Gao, J.; Guo, H.; Ha, S.; Joseph-Mccarthy, D.; Kuchnir, L.; Kuczera, K.; Lau, F. T. K.; Mattos, C.; Michnick, S.; Ngo, T.; Nguyen, D. T.; Prodhom, B.; W. E. Reiher, I.; Roux, B.; Schlenkrich, M.; Smith, J. C.; Stote, R.; Straub, J.; Watanabe, M.; Wiorkiewicz-Kuczera, J.; Yin, D.; Karplus, M. All Atom Empirical Potential for Molecular Modeling and Dynamics Studies of Proteins. *J. Phys. Chem. B* **1998**, *102*, 3586−3616.

(53) Kubelka, J.; Keiderling, T. A. Ab Initio Calculation of Amide Carbonyl Stretch Vibrational Frequencies in Solution with Modified Basis Sets. 1. *N*-Methyl Acetamide. *J. Phys. Chem. A* **2001**, *105*, 10922−10928.

(54) Brooks, B. R.; Brooks, C. L., III; Mackerell, A. D., Jr.; Nilsson, L.; Petrella, R. J.; Roux, B.; Won, Y.; Archontis, G.; Bartels, C.; Boresch, S.; Caflisch, A.; Caves, L.; Cui, Q.; Dinner, A. R.; Feig, M.; Fischer, S.; Gao, J.; Hodoscek, M.; Im, W.; Kuczera, K.; Lazaridis, T.; Ma, J.; Ovchinnikov, V.; Paci, E.; Pastor, R. W.; Post, C. B.; Pu, J. Z.; Schaefer, M.; Tidor, B.; Venable, R. M.; Woodcock, H. L.; Wu, X.; Yang, W.; York, D. M.; Karplus, M. CHARMM: The Biomolecular Simulation Program. *J. Comput. Chem.* **2009**, *30*, 1545−1614.

(55) van Gunsteren, W.; Berendsen, H. Algorithms for macro-molecular dynamics and constraint dynamics. *Mol. Phys.* **1977**, 1311−1327.

(56) Berendsen, H. J. C.; Postma, J. P. M.; van Gunsteren, W. F.; DiNola, A.; Haak, J. R. Molecular dynamics with coupling to an external bath. *J. Chem. Phys.* **1984**, *81*, 3684−3690.

(57) Sagui, C.; Pedersen, L. G.; Darden, T. A. Towards an accurate representation of electrostatics in classical force fields: Efficient implementation of multipolar interactions in biomolecular simulations. *J. Chem. Phys.* **2004**, *120*, 73.

(58) Owrutsky, J. C.; Raftery, D.; Hochstrasser, R. M. Vibrational Relaxation Dynamics in Solutions. *Annu. Rev. Phys. Chem.* **1994**, *45*, 519−555.

(59) Jeon, J.; Cho, M. Redistribution of carbonyl stretch mode energy in isolated and solvated N-methylacetamide: Kinetic energy spectral density analyses. *J. Chem. Phys.* **2011**, *135*, 214504.

(60) Wilk, M. B.; Gnanadesikan, R. Probability plotting methods for the analysis for the analysis of data. *Biometrika* **1968**, *55*, 1−17.

(61) Nienhaus, K.; Lutz, S.; Meuwly, M.; Nienhaus, G. U. Reaction-Pathway Selection in the Structural Dynamics of a Heme Protein. *Chem.—Eur. J.* **2013**, *19*, 3558−3562.